

Bimanual Manipulation Workspace Analysis of Humanoid Robots with Object Specific Coupling Constraints

William Thibault^{1*}

Vidyasagar Rajendran^{2*}

Katja Mombaur³

Abstract—In this work, a bimanual manipulation workspace analysis for humanoid robots is developed. This analysis considers manipulability and whole-body stability for a workspace where constraints exist between the hands of the humanoid for varying hand positions and object grasps. With this goal in mind, a combined manipulability-stability metric based on the volume of the manipulability ellipsoid and the distance of the capture point from the edge of the support polygon is proposed. This metric is visualized in a variety of workspace scenarios including those where the humanoid’s center of mass is moving at a certain velocity and where it is grasping and carrying objects of different masses and shapes. With a focus on tightly coupled bimanual manipulation of varying symmetry, objects studied include boxes, a broom and a rolling pin. A general workspace and a box manipulation workspace are visualized for both the REEM-C and TALOS humanoids showing differences in the generated workspace volumes due to the varying topologies of the humanoids. These visualizations aim to provide insights into how manipulability and whole-body stability are affected by bimanual manipulation scenarios and to inform complex manipulation applications in areas such as control and cost-based planning.

I. INTRODUCTION

With the integration of robots into our daily lives, bimanual or dual-arm robotic manipulation has become increasingly important to manipulate large, heavy and complex shaped objects. Krebs *et al.* [1] identified a number of common bimanual tasks in their dataset created from human motion capture studies including sweeping with a broom, opening juice containers, mixing ingredients for cooking and rolling with a rolling pin. Other tasks requiring bimanual manipulation include lifting boxes, pushing carts and carrying trays. These tasks are well suited for dual-arm robots, especially humanoids, when operating in real-world, human settings (e.g., in a home or factory). However, the complex nature of these high degree of freedom, coordinated, multi-contact tasks result in many challenges in motion planning and control. Bimanual manipulation tasks can be distinguished in terms of hand coordination, coupling and symmetry/asymmetry of the two hands with respect to the object, as suggested in a recent taxonomy developed by

Krebs and Asfour [2]. In this paper, we focus on coordinated, tightly coupled bimanual manipulation cases in which the object imposes clear constraints between the position and orientation of the two hands. We consider objects that introduce symmetric as well as asymmetric grasps, as shown in Figure 1.

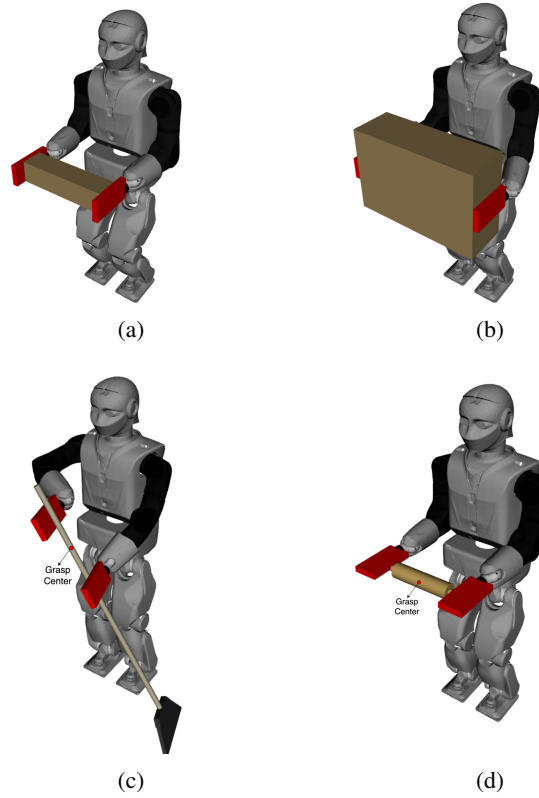


Fig. 1: Examples of objects introducing tightly coupled bimanual manipulation scenarios addressed in this paper: a) a small 1 kg box b) a large 7 kg box c) a sweeping broom (with a left-handed grasp) d) a rolling pin.

A. Related Work

Recent works in the field of bimanual manipulation include learning to identify bimanual tasks from human demonstrations. In [3], the authors learn to identify kitchen related tasks based on the interaction of a person’s hand with different objects. To learn such tasks, a bimanual dataset of 12 motions with 21 household objects was developed for motions such as pouring, stirring and cutting using the measurement of whole-body motion capture data, finger trajectory data, various camera angles and human IMU

* These authors contributed equally and share first authorship.

¹William Thibault is with Department of Mechanical and Mechatronics Engineering, University of Waterloo, Waterloo, ON N2L 3G1, Canada
wcthibau@uwaterloo.ca

²Vidyasagar Rajendran is with the Department of Systems Design Engineering, University of Waterloo, Waterloo, ON N2L 3G1, Canada
vrajendr@uwaterloo.ca

³Katja Mombaur is with the Department of Systems Design Engineering and the Department of Mechanical and Mechatronics Engineering, University of Waterloo, Waterloo, ON N2L 3G1, Canada
katja.mombaur@uwaterloo.ca

data [1]. Another work performs stir-fry cooking with two manipulator arms through learning from demonstration, and online motion generation with one arm relying on visual feedback and the other on a learned Structured-Transformer model [4]. Other methods of developing bimanual motions include control based methods like the projected force-admittance control developed on ARMAR-6 [5]. However, these approaches are often task specific and do not aid in understanding the kinematic complexities involved in highly constrained tasks.

When dealing with multiple manipulators or kinematic trees, such as with humanoids and dual-arm robots, reachability is often considered. One method proposed to allow for humanoids to achieve valid, reachable end poses was the inverse dynamic reachability map (iDRM) method which computes quasi-statically stable poses for an empty workspace offline, then performs a feasibility check during online planning to reach a valid configuration for the desired pose of a hand [6]. An extension of this method for uneven terrain was developed where a blend of forward and inverse dynamic reachability maps are used with the forward approach for the lower body and the inverse approach for the upper body, allowing for non-horizontal plane stances [7]. Another work that treats loco-manipulation of complex contact motions for humanoid robots moving large objects uses a graph search approach for sequencing grasp changes and footsteps while leveraging reachability maps to evaluate the transitions [8].

In relation to reachability maps, workspace analysis can be useful to evaluate poses in a robot's reachable space. A metric such as manipulability, that evaluates how close a robot manipulator is to singularity, is a prime example [9]. One method of measuring bimanual manipulability is the intersection of the individual arm manipulability ellipsoids due to the kinematic constraints imposed on one another [10]. On the topic of bimanual manipulation, Vahrenkamp *et al.* [11] performed a workspace analysis and grasp planning for the ARMAR-III robot. One approach used to determine grasps assessed the bimanual reachability of this robot by considering one hand to be the base link with the other being the tip link creating a 14 degree of freedom chain, which was used to determine reachable grasps with the ability to optimize for a more manipulable grasp. To improve how grasps were selected, an extended manipulability metric was composed using the Yoshikawa manipulability and cost terms for joint limits and obstacle avoidance [12]. One use of this metric with ARMAR-III, was to precompute an inverse reachability map of the robot providing base poses for a required hand pose [13]. Also with the extended manipulability metric, a bimanual workspace analysis for ARMAR-III was performed for a set of spherical coordinates considering the two hands separated a distance around a 3D position [14]. However, ARMAR-III is a stable platform because of the wheeled base design with a low center of mass. Therefore, extensions of this method to humanoids may be insufficient in determining stable, yet manipulable poses.

Moving towards loco-manipulation scenarios with ARMAR-4, a static stability metric, which divides the distance of the projected center of mass from the edge of the support polygon by the distance of the center of the support polygon to its edge, was used to construct stability based reachability maps that help select viable whole-body affordances from a visually perceived environment [15]. The stability metric and the aforementioned extended manipulability metric are combined in a product to create a new metric to better select the whole-body affordances [16]. While this method provides stability considerations that are important when dealing with humanoid robots, it only treats static poses for the first and last pose of a motion using a whole-body controller to move from one to another.

B. Contribution

Despite the extensive research already performed on bimanual manipulation, we have identified a few missing pieces from the perspective of dynamically moving bipedal humanoid robots. The limitations that tight bimanual object grasps impose on the reachable workspace and manipulability of humanoids, the constraints introduced by the object on the hands and collision avoidance have to be explicitly considered to clearly assess bimanual manipulation. In order to be able to plan, optimize and control dynamic (loco-)manipulation motions or to evaluate key points along such motions, the weight and motion of the robot and the manipulated load have to be considered along with whole-body stability beyond the static case. Knowing this, the contributions of our work presented here are:

- A new bimanual manipulability-stability metric that considers the manipulability of a bimanual task and its static and dynamic whole-body stability,
- A workspace analysis with object specific considerations such as mass, collisions and end effector constraints,
- Computations and visualizations of the metric in a variety of workspace scenarios with different example objects and velocities,
- Comparison of two kinematically and dynamically different humanoids, REEM-C and TALOS, in the same manipulation scenario.

II. WORKSPACE METRICS

In this section the metrics used to analyze the workspace of a humanoid are developed, specifically related to manipulability and whole-body stability. Using these individual metrics, a combined metric is defined to analyze the quality of each pose/voxel in the workspace volume of a humanoid.

A. Manipulability

A frequently used metric for measuring manipulability is the volume of the manipulability ellipsoid, also referred to as the Yoshikawa manipulability [9]. For a robotic manipulator with n degrees of freedom in a task space of $q \in \mathbb{R}^m$ with $m \leq n$ and Jacobian J , a square, symmetric and positive

definite matrix A can be defined as:

$$A = JJ^T \in \mathbb{R}^{m \times m}. \quad (1)$$

The eigenvalues λ_i of A correspond to the squares of the singular σ_i values of J . A describes the mapping of a unit sphere in the joint velocity space to end effector velocities, and serves to define the manipulability ellipsoid. The lengths of the half-axes of this ellipsoid are $\sqrt{\lambda_i}$, and the manipulability measure μ for a single manipulator is computed based on its volume as:

$$\mu(A) = \sqrt{\lambda_1 \lambda_2 \dots \lambda_m} = \sqrt{\det A}, \quad (2)$$

$$\mu(J) = \sqrt{\det JJ^T} = \sigma_1 \sigma_2 \dots \sigma_m, \quad (3)$$

where larger values indicate higher manipulability [17]. When considering manipulability in a bimanual manipulation situation, this becomes more challenging, since both end effectors have to be manipulable enough to support a given motion. We therefore extend the metric to select the less manipulable arm which will be the limiting factor:

$$c_m = \min(\mu(A_{\text{LeftArm}}), \mu(A_{\text{RightArm}})). \quad (4)$$

B. Stability

A whole-body stability metric is another important quality value to consider for workspace analysis of humanoids. A reachable and manipulable pose is only useful if the humanoid is also stable. Often, a simple confirmation of stability for a static pose is checking if the ground projected center of mass (GPCM) lies within the support polygon. In [15], a quality metric for stability was proposed based on the distance of the GPCM to the edge of the support polygon. For non-static poses, the capture point can be used as it considers the orbital energy of the linear inverted pendulum model (LIPM) when the center of mass is moving at a velocity to determine if a step needs to be taken [18].

For a 3D LIPM at position r_{CoM} , moving at a velocity of \dot{r}_{CoM} , the instantaneous capture point, r_{ICP} , can be written as follows:

$$r_{\text{ICP}} = P(r_{\text{CoM}} + \frac{\dot{r}_{\text{CoM}}}{\omega_0}), \quad (5)$$

where $P = \begin{bmatrix} 1 & 0 & 0 \\ 0 & 1 & 0 \end{bmatrix}$ is a projection matrix and $\omega_0 = \sqrt{\frac{g}{z_0}}$, where z_0 is a constant center of mass height and g is acceleration due to gravity. Note that if the center of mass is not moving, static stability is preserved [19].

Using the capture point of the robot, a stability metric can be calculated in situations where the center of mass is experiencing a velocity. This metric can be defined as the minimum distance to the edge of the support polygon and is denoted c_s in this work. In the situation where the capture point does not lie within the support polygon, the pose is considered unstable for the current stance and not a valid reachable pose without taking another step. Note that in the case of static poses, the capture point criterion automatically reduces to the static stability criterion on the GPCM.

C. Combined Manipulability-Stability Metric

In order to have a single metric to evaluate different reachable poses in a workspace, a combined manipulability-stability metric must be defined. To create such a metric, [Equation 4](#) and c_s should be normalized by the largest value found for each metric in the workspace analysis to allow for comparison on a similar scale. The normalization is written as:

$$c'_{m_i} = \frac{c_{m_i}}{\max(c_{m_0}, c_{m_1}, \dots, c_{m_n})}, \quad (6)$$

$$c'_{s_i} = \frac{c_{s_i}}{\max(c_{s_0}, c_{s_1}, \dots, c_{s_n})}, \quad (7)$$

where n is the number of reachable poses/voxels in a workspace volume and i indicates the i^{th} reachable voxel from 0 to n .

With the normalized metrics in [Equation 6](#) and [7](#), a combined manipulability metric at a reachable voxel can be defined as a weighted sum of the two metrics as follows:

$$c_{v_i} = \alpha c'_{m_i} + \beta c'_{s_i}, \quad (8)$$

where α and β are weights between 0 and 1 that together sum to 1. Equal weighting for the two metrics is used for the initial evaluation of the metric in this work. In the implementation of this metric, detailed in [Section III](#), we perform a hard check and discard any reachable poses that are unstable.

III. WORKSPACE ANALYSIS METHODOLOGY

A. Whole-body Inverse Kinematics

This work considers humanoid robots, which kinematically have a tree like structure, unlike the chain structure of typical articulated manipulators. This requires a different approach to solving the inverse kinematics (IK) problem of reaching a certain pose in space, especially when considering multiple end effectors and whole-body stability. In this work, we use the EXOTica (Extensible Optimization Toolset) framework by Ivan *et al.* [20] to solve the whole-body inverse kinematics problem for the humanoid using an optimization approach. The optimization problem is set up using task maps that build the cost function and constraints. The task maps include considerations for joint limits, end effector positions and center of mass position, among others. The task maps used for the whole-body IK optimization are described in [Table I](#).

Using these task maps, queries for poses of the tool center point (TCP) of the left and right hand of the humanoid are performed. In this work, we predominantly use the REEM-C humanoid "Seven" by PAL Robotics, from the University of Waterloo. [Figure 2a](#) shows the model of Seven with the left and right TCPs labeled. The task map weights were set with joint limit avoidance as highest priority, followed by stability considerations (restricting the position of the feet, avoiding unnecessary CoM motion) and finally achieving desired end effector poses. For the IK procedure, we used the ExoticaWholeBodyIKConfig problem type with the SciPyEndPoseSolver (using the L-BFGS-B optimization method).

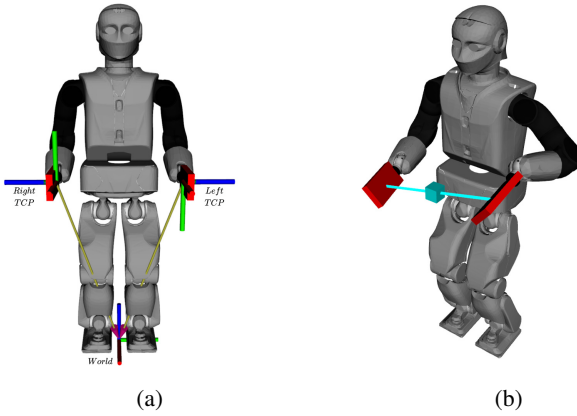


Fig. 2: a) The REEM-C humanoid with *World* frame and left and right TCP frames labeled. Here x is in red, y is in green and z is in blue. b) For the general workspace generation case, a single point on the workspace grid encodes the center between the two end effectors of the robot.

B. Generation of a General Bimanual Workspace Map

For a general bimanual workspace analysis, that will serve as a reference for the results to be presented, the method applied is similar to that of [14]. No specific object is defined in this case, so constraints on distance and orientation of the hands are not applied. For each end effector center point, a range of hand distances and positions around the point are evaluated. This workspace generation procedure discretizes a task space in front of the robot, the area where humanoids perform the majority of their manipulation related motions, into a 6D voxelized workspace. A general workspace analysis is performed for points in a 3D grid and for a series of spherical coordinates around each point. A 3D position vector describes the center between the two end effectors and a spherical coordinate (r, θ, ϕ) encodes the distance between the end effectors as shown in Figure 2b. This description does not store any information about the relative end effector orientation. By removing the orientation of the end effectors, a significant speedup is achieved due to the simplicity of position-only inverse kinematics. We

define $j = [v_0, v_1, v_2]$ as the position of a 6D voxel v that encodes the relation between the two end effectors of the humanoid, represented in the *World* frame (as pictured in Figure 2a). From the spherical coordinates $s = [r, \theta, \phi]$ a Cartesian position $j' = [x', y', z']$ can be derived as $x' = r \sin(\theta) \cos(\phi)$, $y' = r \sin(\theta) \sin(\phi)$ and $z' = r \cos(\theta)$. The Cartesian positions of the left and right TCPs are then given as: $TCP_{left} = j + j'$, $TCP_{right} = j - j'$. Therefore, the spherical coordinates allow the hands to be positioned around the point at different distances, where the TCPs are always considered to be across from each other. During generation, the IK solution is considered valid if the bimanual configuration is reachable, the capture point is within the support polygon, the configuration is collision-free and it respects all joint limits. These hard checks are performed because the cost-based optimization approach for whole-body inverse kinematics, detailed in Subsection III-A, does not have any hard constraints and may converge to infeasible solutions.

C. Generation of Bimanual Workspace Maps under Object-induced Constraints

The workspace maps generated by the approach presented in the previous section give an overly optimistic picture of the situation when it comes to bimanual manipulation of a given object. An object introduces different kinds of constraints:

- the distance of the hands are fixed to the grasping width of the object,
- the orientation of the hands with respect to each other is determined by the grasp required for the object,
- for certain objects, there may be additional constraints on their orientation, e.g. crates that have to be carried upright (fixed roll and pitch).

In this section, we therefore consider an object specific workspace analysis for humanoid bimanual manipulation. In a similar manner, the workspace generation produces a discretized area in front of the robot; however, the 6D voxelized parameters now consider the position and orientation. The object specific workspace requires specific offsets for each TCP based on the grasp for the object rather than using spherical coordinates with position-only IK. In this case, full position and orientation IK is required to meet the grasp requirements. The addition of orientation then allows for the consideration of the object rotation at each position in the workspace, which may be useful depending on the task the robot is performing.

[Algorithm 1](#) provides the details on generating the object specific workspace maps. The algorithm takes as input the range of each voxel dimension, the discretization, the velocity of the center of mass and the object geometry. It then computes the metric c_v ([Equation 8](#)) for each voxel in the defined workspace. Note that in this workspace generation, the object influences the kinematic grasp, the dimensions of the object are considered for collision-checking and the mass of the object is considered for stability. The hands are simplified end effectors for faster computation, and we assume simplified fixed contact grasps.

TABLE I: EXOTica Task Maps used for whole-body inverse kinematics.

Task Map	Formulation
Joint position	$\Phi_{Ref}(\mathbf{x}) = \mathbf{x} - \mathbf{x}_{ref}$
Joint limits	$\Phi_{Bound}(x) = \begin{cases} x - x_{min} - \epsilon, & \text{if } x < x_{min} + \epsilon \\ x - x_{max} + \epsilon, & \text{if } x > x_{max} - \epsilon \\ 0, & \text{otherwise} \end{cases}$
End effector frame	$\Phi_{EffFrame}(x) = \mathbf{M}_A^B$ where $\mathbf{M}_A^B \in SE(3)$
End effector position	$\Phi_{EffPos}(x) = \mathbf{P}_A^B$ where $\mathbf{P}_A^B \in \mathbb{R}^3$
End effector orientation	$\Phi_{EffRot}(x) = \mathbf{R}_A^B$ where $\mathbf{R}_A^B \in SO(3)$
Center of mass	$\Phi_{CoM}(\mathbf{x}) = \left(\sum_i (\mathbf{P}_{CoM_i}^{\text{world}} m_i) \right) / M$

Algorithm 1 Object Bimanual Workspace Generation

Input: $x, y, z, roll, pitch, yaw$ ranges and discretization steps, \dot{r}_{CoM} , object_geometry

Parameters:

```

1: for  $x \in \{x_{min}, \dots, x_{max}\}$  do
2:   for  $y \in \{y_{min}, \dots, y_{max}\}$  do
3:     for  $z \in \{z_{min}, \dots, z_{max}\}$  do
4:       for  $roll \in \{roll_{min}, \dots, roll_{max}\}$  do
5:         for  $pitch \in \{pitch_{min}, \dots, pitch_{max}\}$  do
6:           for  $yaw \in \{yaw_{min}, \dots, yaw_{max}\}$  do
7:              $j \leftarrow \text{Vector}(x, y, z, roll, pitch, yaw)$ 
8:              $ji, jr \leftarrow \text{calcGraspOffsets}(\text{object\_geometry})$ 
9:              $q \leftarrow \text{calcBothArmsIK}(j + ji, j + jr)$ 
10:            stateValid  $\leftarrow \text{isStateValid}(q)$ 
11:            if stateValid then
12:               $c'_m \leftarrow \text{calcNormManipulability}(q)$ 
13:               $c'_s \leftarrow \text{calcNormStability}(q, \dot{r}_{CoM})$ 
14:               $c_v \leftarrow \alpha c'_m + \beta c'_s$ 
15:              writeVoxelToDatabase( $x, y, z, roll, pitch, yaw, c_v$ )

```

D. Workspace Visualization

The generated results for c_v at each voxel in the workspace are visualized by a color spectrum ranging from low quality in blue to high quality in yellow/orange (going through green as medium quality). Any unreachable or unstable voxel is plotted as gray. As multiple results appear at each 3D voxel, the average result is displayed through an overlap of voxels by applying a transparency.



Fig. 3: The metric color range used throughout this work.

IV. RESULTS

In this section we present various workspace scenarios to illustrate our proposed metric in the context of bimanual manipulation with humanoids.

A. General Workspace Maps

For the general case, generated as described in [Subsection III-B](#), a 0.8 m^3 workspace with 5 cm voxel discretization is considered. The workspace is predominantly in front of the robot where most manipulation tasks take place and no CoM velocity is considered. [Figure 4](#) shows the full workspace considered in the first row and a horizontal cut through in the second row. [Figure 4a](#) and [4d](#) show the manipulability distribution (i.e., $\alpha = 1$ and $\beta = 0$ in [Equation 8](#)). As can be seen, voxels closer to the REEM-C are of higher manipulability while voxels near the edge of the workspace are of lesser manipulability. This is to be expected given that the further the arms extend, the closer they are to singularity (and the less manipulable the configuration will be). [Figure 4b](#) and [4e](#) shows the stability distribution of the workspace ($\alpha = 0$ and $\beta = 1$ in [Equation 8](#)). The REEM-C is relatively stable for this cut through with voxels near the edges being of lower quality. This is expected given that the REEM-C would need to attempt to shift its CoM in order to reach some of these poses, reaching the edge of the support polygon. [Figure 4c](#) and [4f](#) show the combined manipulability-stability metric with weightings, $\alpha = 0.5$ and $\beta = 0.5$. Configurations nearer to the REEM-C are of higher quality. This visualization gives an overview of the most stable and manipulable configurations in the considered workspace. Of all the queried voxels, REEM-C was able to reach 22 % of the workspace.

and $\beta = 0.5$. Configurations nearer to the REEM-C are of higher quality. This visualization gives an overview of the most stable and manipulable configurations in the considered workspace. Of all the queried voxels, REEM-C was able to reach 22 % of the workspace.

B. Workspace Maps with Varying Center of Mass Velocities

As described in our metric formulation in [Subsection II-B](#), we consider the capture point for our stability metric which allows us to account for CoM velocity. Encoding this data into the workspace visualization gives a sense of the robot's capabilities while in motion. To this end, we present exemplary workspaces to show how this consideration affects voxel reachability.

For this example, we consider a small subset of the general workspace presented in [Subsection IV-A](#) and show four workspaces of varying CoM velocities. Here the metric considered is stability (i.e., $\alpha = 0.0$ and $\beta = 1.0$ in [Equation 8](#)). First, in [Figure 5a](#), we show a case where no CoM velocity is applied. As can be seen, most of the workspace can be reached and voxels close to the REEM-C are of higher quality. When a CoM velocity is applied in the x -direction, a portion of the workspace becomes unreachable due to the capture point exiting the support polygon, as shown in [Figure 5b](#). Similarly, [Figure 5c](#) shows the scenario when a CoM velocity in the y -direction is applied. A portion of the workspace in the y -direction again, becomes unreachable. Applying a CoM velocity with both x and y components shows that only a small corner of the workspace is now reachable. This information could be useful when considering CoM velocity in humanoid motion planning scenarios.

C. Workspace Maps with Different Object Masses

In this section we show two workspace scenarios where the REEM-C manipulates boxes. Box dimensions are taken into consideration for collision-checking and box mass is taken into account for the stability metric.

The first scenario involves a light 1 kg box of dimensions $0.1 \text{ m} \times 0.4 \text{ m} \times 0.1 \text{ m}$. The workspace checked for this scenario was 0.8 m^3 with a translational discretization of 5 cm and a rotational discretization of 15° . [Figure 6](#) shows cut throughs of the workspace. We can see that the workspace is fairly symmetric which is expected given that the box being manipulated is held with a symmetric grasp. The impact of carrying even this light box can be seen in the reduction of the feasible workspace in the x -direction. The outer voxels are infeasible due to the capture point existing the support polygon which violates our currently developed metric. For this case, the feasible area of the checked workspace was 18 % which is a reduction from the general workspace shown in [Subsection IV-A](#).

The second scenario is manipulating a bigger box with dimensions $0.2 \text{ m} \times 0.6 \text{ m} \times 0.4 \text{ m}$, weighing 7 kg. From [Figure 7](#) we can see that the effect of the increased box mass has a significant impact on the feasible workspace volume. For this case, the feasible area of the checked workspace

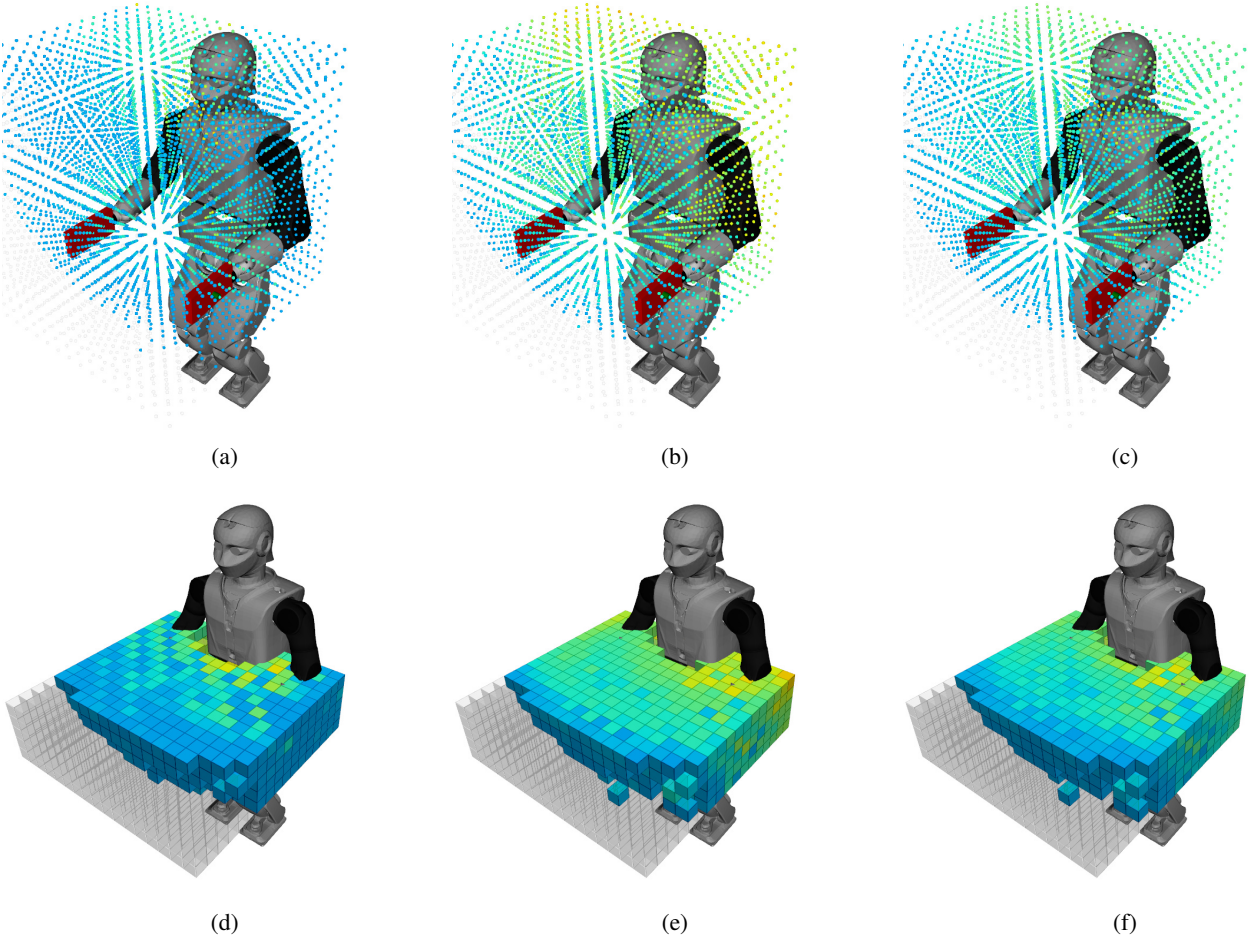


Fig. 4: Visualizations of the workspace considered for the general case. Low quality voxels are blue and high quality voxels are yellow/orange. Voxels that are unreachable or unstable are translucent grey. The first row shows the workspace that was considered and the second row shows a horizontal cut through. a) and d) show the manipulability metric, b) and e) show the stability metric and c) and f) show the combined manipulability-stability metric as detailed in Equation 8.

was 10 %, a reduction from the 1 kg box case. We can see in Figure 7a, even holding the box at a distance of 0.2 m–0.3 m from the torso brings the capture point (shown as a green dot between the feet) close to the edge of the support polygon (shown in blue outline).

D. Workspace Maps with Different Objects

In this section we consider two other objects with different grasping configurations, a rolling pin and a broom.

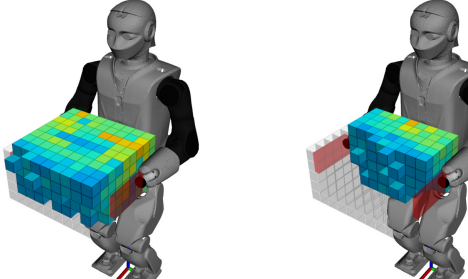
For the rolling pin, we considered a small workspace in front of the robot and restricted the orientation of the rolling pin to 7.5° around all axes. Pictured in Figure 8a, is the rolling pin workspace at a height of $z = 0.9$ m from the ground. The middle portion of the workspace in the x -direction is reachable but the edges closer to the robot and away from the robot are unreachable. The edges further away being unreachable is due to the fact that the arms and torso must extend and tilt causing stability issues. For the area closer to the robot, reachability is degraded due to self-collisions of the arms with the torso. When visualizing a higher z value, at 1.1 m, we can see that much more

of the workspace is reachable due to the elbows pointing outwards from the torso, avoiding self-collisions. Thus, from this workspace, we can see the effects of having this grasp constraint and how it restricts motion at lower heights while standing in one place. We note that contacts and force are not considered in this workspace, and we are purely evaluating the kinematics of this constrained bimanual task.

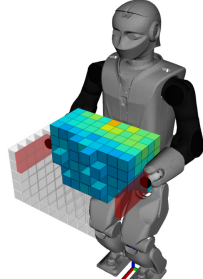
For the broom, we considered a left-handed grasp with the right hand of the REEM-C above the left hand. Figure 9 shows two cut throughs of the workspace. Importantly, from Figure 9b, we see that the area towards the left side of the REEM-C is of higher quality and reachable where as much of the right side is unreachable. This is expected since the robot would have to reach across its body with the left hand to access the right side of the workspace, causing collisions with the torso.

E. Workspace Maps of TALOS

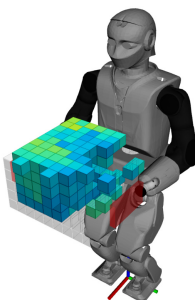
Finally, we show a few workspace scenarios with the TALOS humanoid. Figure 10 shows cut throughs of the manipulability-stability distribution for a general workspace,



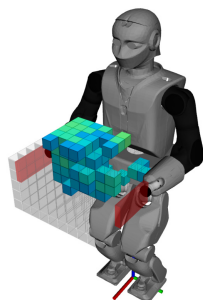
(a)



(b)

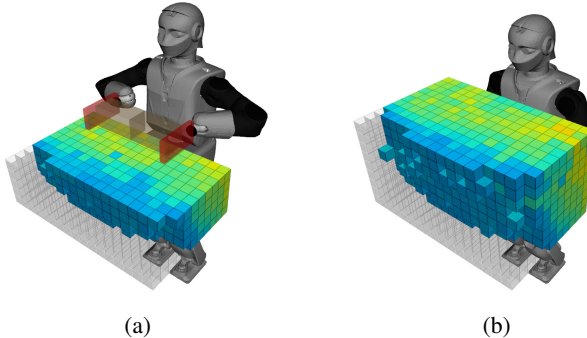


(c)

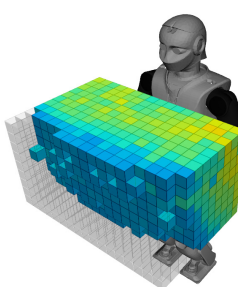


(d)

Fig. 5: Visualizations of different CoM velocity (m/s) cases for a subset of the general workspace using the stability metric. a) $\dot{r}_{CoM} = [0.0, 0.0, 0.0]$ b) $\dot{r}_{CoM} = [0.2, 0.0, 0.0]$ box c) $\dot{r}_{CoM} = [0.0, 0.6, 0.0]$ d) $\dot{r}_{CoM} = [0.2, 0.6, 0.0]$.



(a)

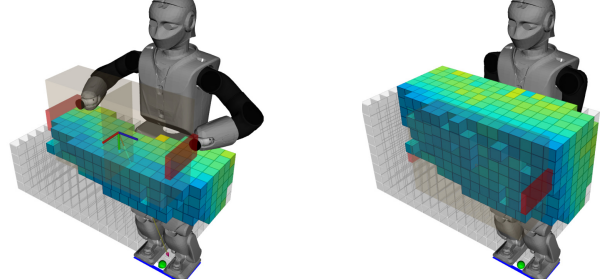


(b)

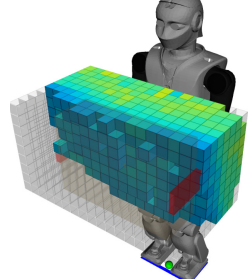
Fig. 6: Visualization of the bimanual manipulability-stability metric for the REEM-C manipulating a 1 kg box. a) A cut through at $z = 1.0$ m b) A cut through at $z = 1.2$ m.

generated with spherical coordinates as described in [Subsection III-B](#). We used the same workspace volume and discretization parameters as was done for the REEM-C in [Figure 4](#). We see that voxels nearer to TALOS are of higher quality while the edges of the generated workspace are of lower quality. Notably, as compared to the REEM-C, TALOS was able to reach 34 % of the queried voxels as compared to the REEM-C's 22 %. This is expected given that TALOS has longer arms and a shoulder topology that allows more motion than the REEM-C.

We also consider the same 1 kg box that was considered for the REEM-C in [Subsection IV-C](#) for the TALOS, as

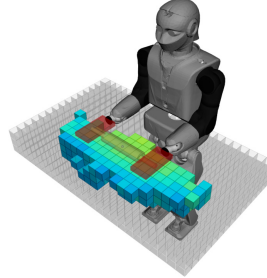


(a)

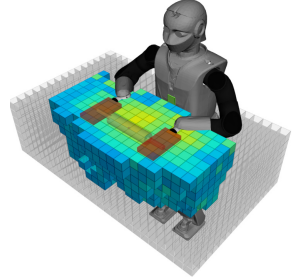


(b)

Fig. 7: Visualization of the bimanual manipulability-stability metric for the REEM-C manipulating a 7 kg box. a) A cut through at $z = 1.0$ m b) A cut through at $z = 1.2$ m.



(a)



(b)

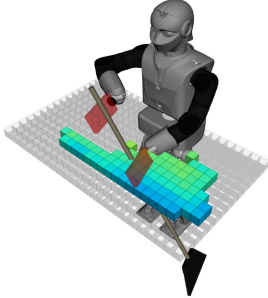
Fig. 8: Visualization of the bimanual manipulability-stability distribution for REEM-C manipulating a rolling pin. a) A cut through at $z = 0.9$ m b) A cut through at $z = 1.1$ m.

shown in [Figure 11](#). Notably, TALOS was able to reach 26 % of the checked volume whereas the REEM-C was only able to reach 18 %. Again, this is due to the differences in limb lengths and topology.

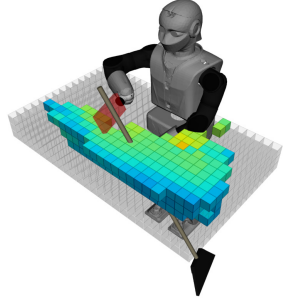
V. CONCLUSIONS AND OUTLOOK

In this work, a bimanual manipulation workspace analysis was developed for humanoid robots, that considers a combined manipulability-stability metric based on the volume of the manipulability ellipsoid and the distance of the capture point from the edge of the support polygon. A general workspace was generated and visualized for the REEM-C as well as specific object workspace analyses for boxes, a broom and a rolling pin. Additionally, workspaces with varying CoM velocities were compared and the workspace differences between REEM-C and TALOS were analyzed. These workspace analyses provide valuable insight into how well a humanoid robot can manipulate an object with two hands and in turn help inform motions for a variety of applications from household chores to warehouse tasks.

Future work involves developing a cost based planner to use the manipulability-stability metric to compute optimal motions. Another area of focus is developing a more complex stability metric that considers angular momentum with the zero moment point for the LIPM. We also intend to investigate the effect of contacts on the manipulability-stability metric in various locomotion scenarios.

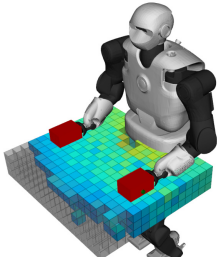


(a)

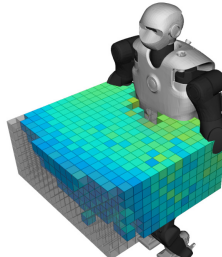


(b)

Fig. 9: Visualization of the bimanual manipulability-stability distribution for REEM-C manipulating a broom. a) A cut through at $z = 0.9$ m b) A cut through at $z = 1.0$ m.



(a)



(b)

Fig. 10: Visualization of the bimanual manipulability-stability distribution for the TALOS humanoid, for the general case with spherical coordinates as described in Subsection III-B. a) A cut through at $z = 0.9$ m b) A cut through at $z = 1.1$ m.

ACKNOWLEDGMENT

We acknowledge the support of the Natural Sciences and Engineering Research Council of Canada (NSERC), the Tri-Agency Canada Excellence Research Chair Program, and the University of Waterloo.

REFERENCES

- [1] F. Krebs, A. Meixner, I. Patzer, and T. Asfour, “The kit bimanual manipulation dataset,” in *2020 IEEE-RAS 20th International Conference on Humanoid Robots (Humanoids)*, 2021, pp. 499–506.
- [2] F. Krebs and T. Asfour, “A bimanual manipulation taxonomy,” *IEEE Robotics and Automation Letters (RA-L)*, vol. 7, no. 4, pp. 11 031–11 038, 2022.
- [3] C. R. G. Dreher, M. Wächter, and T. Asfour, “Learning object-action relations from bimanual human demonstration using graph networks,” *IEEE Robotics and Automation Letters*, vol. 5, no. 1, pp. 187–194, 2020.
- [4] J. Liu, Y. Chen, Z. Dong, S. Wang, S. Calinon, M. Li, and F. Chen, “Robot cooking with stir-fry: Bimanual non-prehensile manipulation of semi-fluid objects,” *IEEE Robotics and Automation Letters*, vol. 7, no. 2, pp. 5159–5166, 2022.
- [5] J. Gao, Y. Zhou, and T. Asfour, “Projected force-admittance control for compliant bimanual tasks,” in *2018 IEEE-RAS 18th International Conference on Humanoid Robots (Humanoids)*, 2018, pp. 1–9.
- [6] Y. Yang, V. Ivan, Z. Li, M. Fallon, and S. Vijayakumar, “idrm: Humanoid motion planning with realtime end-pose selection in complex environments,” in *2016 IEEE-RAS 16th International Conference on Humanoid Robots (Humanoids)*, 2016, pp. 271–278.
- [7] Y. Yang, W. Merkt, H. Ferrolho, V. Ivan, and S. Vijayakumar, “Efficient humanoid motion planning on uneven terrain using paired forward-inverse dynamic reachability maps,” *IEEE Robotics and Automation Letters*, vol. 2, no. 4, pp. 2279–2286, 2017.
- [8] M. Murooka, I. Kumagai, M. Morisawa, F. Kanehiro, and A. Kheddar, “Humanoid loco-manipulation planning based on graph search and reachability maps,” *IEEE Robotics and Automation Letters*, vol. 6, no. 2, pp. 1840–1847, 2021.
- [9] T. Yoshikawa, “Manipulability and redundancy control of robotic mechanisms,” in *Proceedings. 1985 IEEE International Conference on Robotics and Automation*, vol. 2, 1985, pp. 1004–1009.
- [10] S. Lee, “Dual redundant arm configuration optimization with task-oriented dual arm manipulability,” *IEEE Transactions on Robotics and Automation*, vol. 5, no. 1, pp. 78–97, 1989.
- [11] N. Vahrenkamp, M. Przybylski, T. Asfour, and R. Dillmann, “Bimanual grasp planning,” in *2011 11th IEEE-RAS International Conference on Humanoid Robots*, 2011, pp. 493–499.
- [12] N. Vahrenkamp, T. Asfour, G. Metta, G. Sandini, and R. Dillmann, “Manipulability analysis,” in *2012 12th IEEE-RAS International Conference on Humanoid Robots (Humanoids 2012)*, 2012, pp. 568–573.
- [13] N. Vahrenkamp, T. Asfour, and R. Dillmann, “Robot placement based on reachability inversion,” in *2013 IEEE International Conference on Robotics and Automation*, 2013, pp. 1970–1975.
- [14] N. Vahrenkamp and T. Asfour, “Representing the robots workspace through constrained manipulability analysis,” *Autonomous Robots*, vol. 38, pp. 1–14, 01 2014.
- [15] P. Kaiser, D. González-Aguirre, F. Schültje, J. Borràs, N. Vahrenkamp, and T. Asfour, “Extracting whole-body affordances from multimodal exploration,” in *2014 IEEE-RAS International Conference on Humanoid Robots*, 2014, pp. 1036–1043.
- [16] P. Kaiser, N. Vahrenkamp, F. Schültje, J. Borràs, and T. Asfour, “Extraction of whole-body affordances for loco-manipulation tasks,” *International Journal of Humanoid Robotics*, vol. 12, p. 1550031, 06 2015.
- [17] K. M. Lynch and F. C. Park, *Modern Robotics: Mechanics, planning, and Control*. Cambridge, United Kingdom: Cambridge University Press, 2019, ch. 5.4 Manipulability, pp. 196–199.
- [18] J. Pratt, J. Carff, S. Drakunov, and A. Goswami, “Capture point: A step toward humanoid push recovery,” in *2006 6th IEEE-RAS International Conference on Humanoid Robots*, 2006, pp. 200–207.
- [19] J. E. Pratt, S. Bertrand, and T. Koolen, *Stepping for Balance Maintenance Including Push-Recovery*. Dordrecht: Springer Netherlands, 2019, pp. 1419–1466. [Online]. Available: https://doi.org/10.1007/978-94-007-6046-2_41
- [20] V. Ivan, Y. Yang, W. Merkt, M. P. Camilleri, and S. Vijayakumar, “EXOTica: An Extensible Optimization Toolset for Prototyping and Benchmarking Motion Planning and Control,” in *Robot Operating System (ROS)*, A. Koubaa, Ed. Cham: Springer International Publishing, 2019, vol. 778, pp. 211–240, series Title: Studies in Computational Intelligence. [Online]. Available: http://link.springer.com/10.1007/978-3-319-91590-6_7